Journal of Quantitative Spectroscopy & Radiative Transfer 323 (2024) 109054

Contents lists available at ScienceDirect

Journal of Quantitative Spectroscopy and Radiative Transfer

journal homepage: www.elsevier.com/locate/jqsrt

A light scattering model for large particles with surface roughness

H. Ballington *, E. Hesse

Atmospheric and Climate Physics Group, Department of Physics, Astronomy & Mathematics, School of Physics, Engineering & Computer Science, University of Hertfordshire, United Kingdom

ARTICLE INFO

Keywords:
Light scattering
Physical optics
Surface roughness
Diffraction

ABSTRACT

A physical-optics hybrid method designed for the computation of single-scattering properties of particles with complex shapes, including surface roughness, is presented. The method applies geometric optics using a novel ray backtracing algorithm to compute the scattered field on the particle surface. A surface integral equation based on the equivalence theorem is used to compute the scattered far-field, which yields the full Mueller matrix and integrated single-scattering parameters. The accuracy is tested against the discrete dipole approximation for fixed orientation smooth and roughened compact hexagonal columns for 3 values of refractive index. The method is found to compute asymmetry parameter, and scattering and extinction efficiencies with mean errors of −1.0%, −1.4%, −1.2%, respectively, in a computation time reduced by 3 orders of magnitude. The work represents a key step forwards for modelling particles with physical surface roughness within the framework of physical-optics and provides a versatile tool for the fast and quantitative study of light scattering from non-spherical particles with size much larger than the wavelength.

1. Introduction

In the field of light scattering, theoretical models for single scattering stand as an indispensable tool with far-reaching applications. Calibration of laboratory instrumentation often relies on theoretical calculations, and the discernment of cell health or disease in biomedical testing is significantly informed by the examination of single scattering properties [1,2]. Occupational health applications include the monitoring of dust size as a means of preventing dust explosions in coal mines and other settings [3], as well as for the recording of hazardous substances such as asbestos [4] and flour dust [5]. Weather and climate models rely on single scattering parameters as essential inputs to radiative transfer computations [6], which are important for understanding and predicting the Earth's climate system. A quantitative analysis of light scattering can provide a useful tool for applications with specific angular detection ranges and resolution. For example, the instruments of the Small Ice Detector family [7] detect light scattered in the region between 6° and 25° from the forwards direction, while light detection and ranging (LIDAR) instruments detect direct backscattering. An array of applications are focused on the inversion problem, where theoretical models are employed alongside experimental data to determine the size, shape, and particle complexity of a scatterer [8]. Two-wavelength detection can provide information about particle size and aid in discrimination of clouds and aerosols, as well as the identification of aerosol types [9]. Another important application includes multiple scattering calculations for determining irradiances in climate studies and radiances in remote sensing. The accurate calculation of scattering matrices and integrated parameters, including single scattering albedo, asymmetry parameter, and scattering and extinction cross sections and efficiencies, remains central to these applications.

For non-spherical particles, several methods for solving the light scattering problem to a high degree of accuracy exist, including T-matrix [10–12], finite-difference time-domain [13–15], and the discrete dipole approximation [16–19]. However, these approaches become computationally expensive as the particle refractive index n and size parameter $X = |\pi d/\lambda|$ increase, where d is the maximum particle dimension and λ is the wavelength. For large particles, several computationally efficient approaches using classical geometric optics (GO) were initially developed [20–24]. Based on a combination of ray-tracing and Fraunhofer diffraction, these methods model the propagation of electromagnetic fields in the short wavelength limit as straight-line paths, which provides an approximate solution to the scattering problem with an accuracy that increases with the minimum dimension of the particle [25]. In recent years, several so-called physical-optics hybrid methods have been developed, which improve upon GO by accounting for additional diffractive effects [26–30]. While these methods have been widely used to model a variety of particle geometries with smooth surfaces, few can be directly applied to model particles with surface roughness. Instead, several approaches

* Corresponding author.
E-mail address: h.ballington@herts.ac.uk (H. Ballington).

https://doi.org/10.1016/j.jqsrt.2024.109054
Received 6 February 2024; Received in revised form 16 May 2024; Accepted 17 May 2024
Available online 19 May 2024

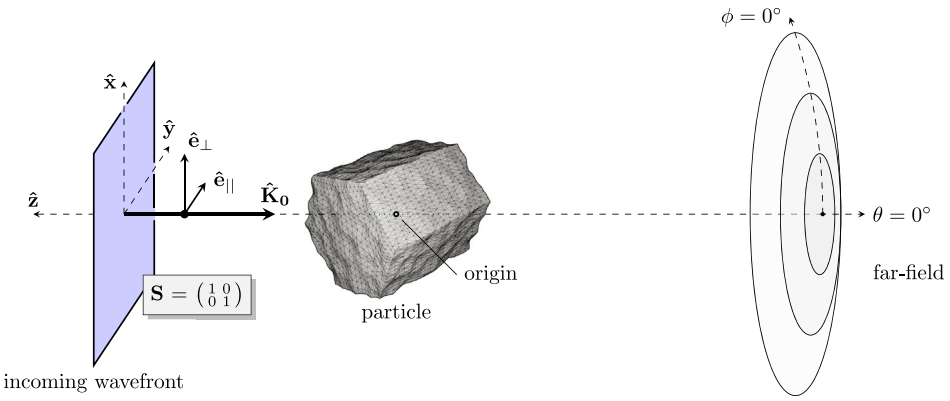

Fig. 1. The scattering geometry. An unpolarised plane wave is incident along the $\hat{\mathbf{z}}$ axis, with perpendicular and parallel electric field vectors defined along the $\hat{\mathbf{x}}$ and $\hat{\mathbf{y}}$ axes, respectively. The particle is positioned with centre of mass on the origin. The far-field is located at a distance R from the origin, with contour lines of constant θ shown for convenience.

are focused on the effects of deviations from perfect particle geometries. For instance, one of the first and now widely used techniques for this is the 'tilted-facets' method, which applies a stochastic distortion to the particle surface [31]. Another approach using distorted smooth particle shapes in order to mimic varying degrees of surface roughness [32], has been implemented in several recent works [33–36]. A physical-optics method based on the subdivision of an incident wave into triangle-shaped beams was also developed that directly modelled strongly absorbing hexagonal prisms with surface roughness [37].

In this work, the open-source parent beam tracer (PBT) method [38] is introduced as a physical-optics hybrid method for directly modelling light scattering by large, non-spherical particles with complex shapes, including those with surface roughness. The scattered field is computed in 2 main steps. First, the near-field on the particle surface is approximated using principles of GO. Improved accuracy is achieved by computing the propagation direction of waves in the near-field zone based on macroscopic features of the particle shape. A novel ray backtracing algorithm is used to attain computational stability for highly complex particle shapes. Second, a surface integral diffraction equation [39] combined with the equivalence theorem [40] is used to map from the near-field on the particle surface to the far-field, where the Mueller matrix and integrated scattering parameters are obtained.

2. Theoretical basis

2.1. Introduction

The PBT is an analytical method for computing the single-scattering of an electromagnetic plane wave incident on any large, non-spherical particle. The particle is assumed to be homogeneous, isotropic, and dielectric. The scattering geometry consists of a particle with centre of mass located at the origin and an illuminating incident plane wave with an electric field given by

$$\mathbf{E}_{inc} = \mathbf{E}_0 e^{ik_0(\hat{\mathbf{K}}_0 \cdot \mathbf{r} - \omega t)}, \tag{1}$$

where $\hat{\mathbf{K}}_0 = -\hat{\mathbf{z}}$ is the propagation vector defined along the $-\hat{\mathbf{z}}$ axis, λ is the wavelength of incident light, $k_0 = -\frac{2\pi}{\lambda}$ is the wavenumber, ω is the angular frequency, and $\mathbf{E}_0$ is the complex amplitude vector. The amplitude scattering matrix $\mathbf{S} = \left(\begin{smallmatrix}S_2 & S_3\\ S_4 & S_1\end{smallmatrix}\right)$ is then introduced, which relates the scattered electric field $\mathbf{E}_{\mathbf{sca}}$ in a particular direction to $\mathbf{E}_{inc}$ by

$$\mathbf{E}_{sca} = \begin{pmatrix} E_{||} \\ E_\perp \end{pmatrix}_{sca} = \begin{pmatrix} S_2 & S_3 \\ S_4 & S_1 \end{pmatrix} \begin{pmatrix} E_{||} \\ E_\perp \end{pmatrix}_{inc}. \tag{2}$$

In the near-field, $\mathbf{S}$ is obtained on the particle surface by a summation over external reflections and transmitted beams which propagate according to GO. In the far-field, the scattered light is assumed to obey the radiation condition [41], and is a transverse, spherical wave that in general depends on the polar and azimuthal scattering angles, θ and ϕ. The forwards scattering direction $\theta = 0°$ is defined to be aligned with the $-\hat{\mathbf{z}}$ axis such that the position of a point at a distance R in the far-field is given by

$$\mathbf{r} = \begin{pmatrix} x \\ y \\ z \end{pmatrix} = \begin{pmatrix} R\sin\theta\cos\phi \\ R\sin\theta\sin\phi \\ -R\cos\theta \end{pmatrix}. \tag{3}$$

The incident field is defined by a plane surface positioned above the particle with a surface normal aligned with $\hat{\mathbf{K}}_0$. For an unpolarised incident plane wave, the amplitude matrix at any point on this surface is defined as the identity matrix, $\mathbf{I} = \left(\begin{smallmatrix}1 & 0\\ 0 & 1\end{smallmatrix}\right)$. The incident amplitude matrix is defined with respect to the yz plane with orthonormal field unit vectors $\hat{\mathbf{e}}_\perp$ and $\hat{\mathbf{e}}_{||}$ along the $\hat{\mathbf{x}}$ and $\hat{\mathbf{y}}$ directions, respectively. A diagram summarising the scattering geometry is shown in Fig. 1.

2.2. Near-field computation

2.2.1. Macroscopic particle features

In a preliminary study, the internal fields of a smooth and a rough compact hexagonal column with refractive index 1.31 + 0i at fixed orientation were compared. The particles were assumed to be homogeneous, dielectric, and isotropic. The internal fields were computed using the discrete dipole approximation (DDA) [19], of which the accuracy has been well studied [42]. The columns were chosen to have hexagonal edge length 2.5 μm and prism length 5 μm, with an incident wavelength of 0.5236 μm. Gaussian random roughness was used for the rough column according to the method given by Collier et al. [43]. A correlation length of 0.25 μm and standard deviation 0.05 μm were chosen to yield a mesoscale roughness without excessive deformation of the overall particle shape. The particles were illuminated with an x-polarised plane wave at normal incidence on one of the basal facets. The computed internal field x-component is shown in Fig. 2. A propagating mode resembling a plane wave is observed, which justifies the use of GO in the near-field zone. Upon visual inspection, it was found that the internal field behaviour was almost identical for both the smooth and rough columns. This led to the idea that, accurate results in a physical-optics hybrid method could be achieved by modelling internally propagating beams as originating from the macroscopic structures of the surface, rather than from individual facets of the mesh. To be more specific, the reflected and refracted propagation direction of beams in the near-field can be computed using macroscopic properties of the particle surface. In this way, the limitations of classical GO when applied to surfaces with features smaller than the wavelength can be mitigated. Based on this proposal, a parent structure is defined within the framework of the PBT as a collection of facets which, when illuminated by a plane wave, produce one reflected (and possibly one

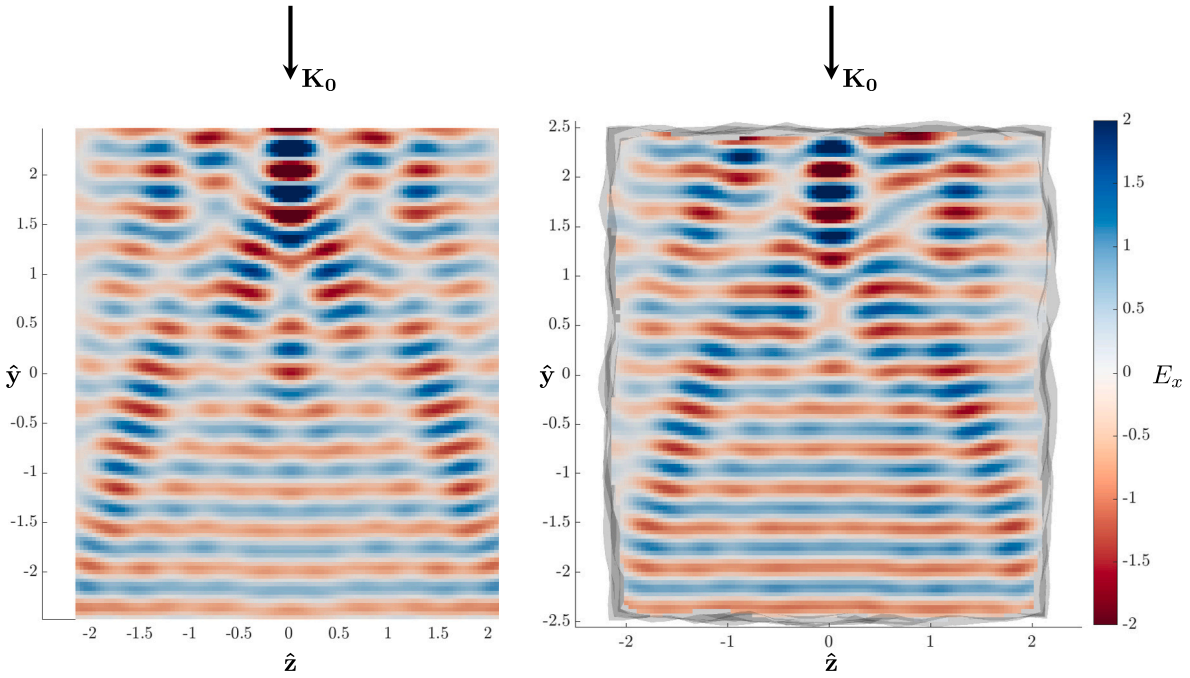

Fig. 2. Internal field x-component for x-polarised normally incident light of wavelength 0.5236 μm for smooth (left) and rough (right) hexagonal columns with aspect ratio 1. Computed with the discrete dipole approximation [19].

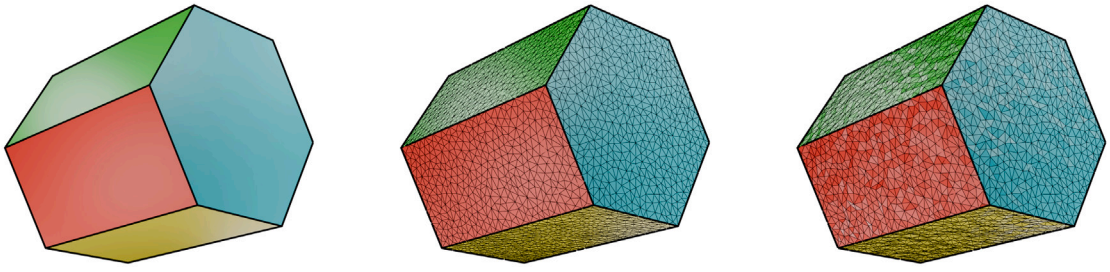

(a) Original, smooth. (b) Meshed, smooth. (c) Meshed, with surface roughness.

Fig. 3. Sequence of steps showing the proposed method for constructing the parent structures, which are represented by different colours.

refracted) wave with a single propagation direction in the near-field. For the case of smooth surfaces with dimension $d \gg \lambda$, this approach simplifies to methods that have already been effectively implemented in many successful physical-optics hybrid methods [40,44,45]. In order to define the parent structures of the surface, the following method is proposed:

1. First, a smooth particle geometry is constructed as shown in Fig. 3(a). Each of the facets represents a parent and should be of dimension much larger than the wavelength to permit the use of GO.
2. Second, each parent facet may then be subdivided into a mesh, where each element of the mesh is a facet assigned to the parent. This is shown in Fig. 3(b).
3. Third, the vertices of the mesh may be displaced according to the desired surface texture, as shown in Fig. 3(c).

It may also be possible to define the parent structures in the opposite direction by starting with a complex-shaped particle mesh and using a mesh simplification algorithm, such as described in [46], to arrive at a simplified mesh representing the parents. However, this approach has not yet been investigated. The surface normal of a parent $\hat{\mathbf{N}}$ is computed as the normalised average of all facet normals $\hat{\mathbf{n}}$ that belong to it. The angle of incidence θ_i between $\hat{\mathbf{N}}$ and the incident propagation direction $\hat{\mathbf{K}}_\mathbf{0}$ is combined with Snell's law to calculate a refracted propagation vector $\hat{\mathbf{K}}'$ at a transmitted angle θ_t and a reflected propagation vector $\hat{\mathbf{K}}''$, which is illustrated in Fig. 4(a). In essence, mesoscopic features of the particle surface are designed to have little effect on the propagation direction of waves in the near-field. However, they have a significant effect on the phase during the near-field beam tracing (Section 2.2.2), and the far-field mapping (Section 2.3).

2.2.2. Beam tracing

A novel beam tracing algorithm is employed in order to attain stability and computational efficiency during the near-field computation for highly complex particle surfaces that can exceed 10^4 facets. In the following method, the notation f^i is used to represent the ith facet of the surface mesh, with $i = \{1, 2, \ldots, N_f\}$, where N_f represents the total number of facets. The amplitude matrix of near-field beams as a function of position are represented by an amplitude matrix at each of the illuminated facets on the particle surface. The amplitude scattering matrix at f^i is denoted by $\mathbf{S^i}$. When a part of the particle surface is illuminated by an incident wave, the amplitude matrix at each facet of the surface is computed. For each illuminated parent structure, a

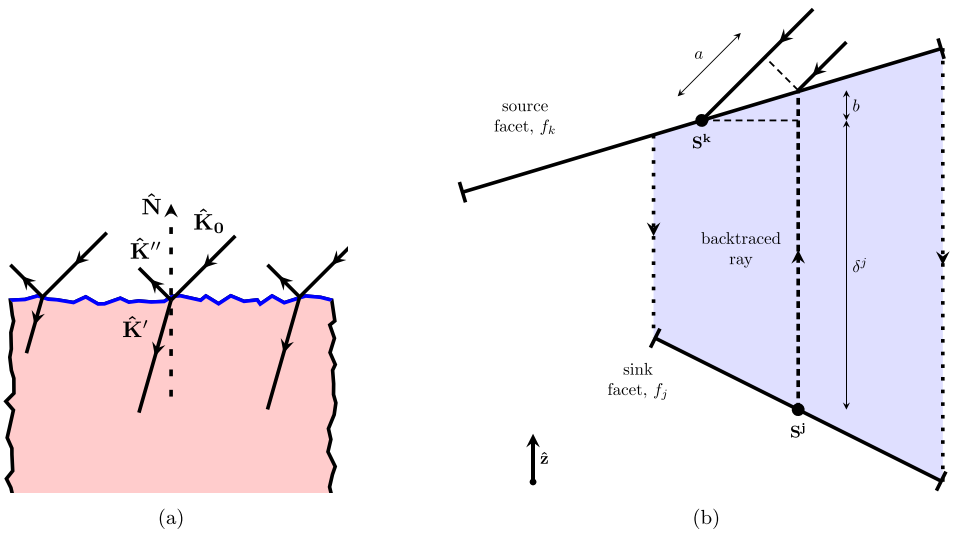

Fig. 4. (a) The average normal of a parent structure (blue) is used to compute a reflected and refracted direction of propagation for rays incident the facets assigned to it. Hence, all the reflected and refracted rays from this surface remain parallel. (b) Beam propagation from a source facet f^k to a sink facet f^j. Facet centroids are represented by black dots. A ray is backtraced from the centroid of f^j and is found to intersect within the bounded cross section of f^k. Edges of the beam are represented by dotted lines. It can be shown that $n_1 a = n_2 b$, and therefore δ^j describes the path length between the centroid of f^k and f^j. The corresponding phase difference relates $\mathbf{S^k}$ to $\mathbf{S^j}$.

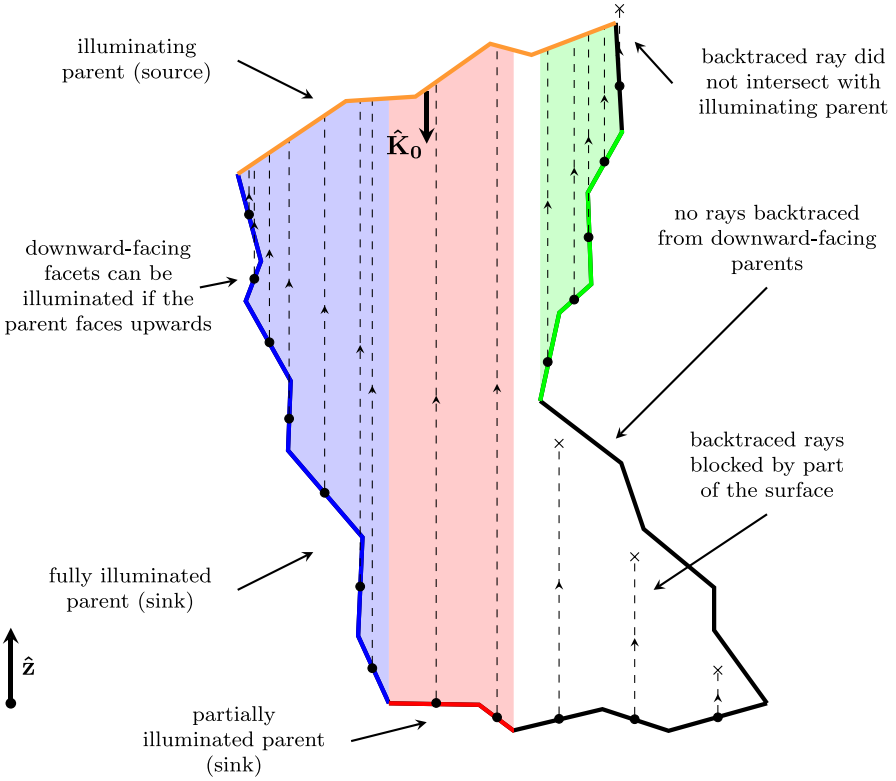

Fig. 5. Visual representation of the ray backtracing algorithm. A beam is emitted along the $-\hat{\mathbf{z}}$ direction from the source facets f^k in the illuminating parent. Rays are then backtraced along the $\hat{\mathbf{z}}$ direction from the centroids of all other facets f^i that belong to upward-facing parents. Unobstructed rays that successfully intersect with the illuminating parent determine the paths along which the beam should propagate. Rays are deliberately allowed to pass through facets of the same parent from which the ray was emitted, which improves accuracy for oblique reflection. Different colours represent collections of rays associated with a particular parent. The scale of surface roughness is exaggerated for clarity.

new reflected and refracted beam is produced. In general, this leads to several beams which are propagated in a recursive process. Apart from the initial illumination by an external plane wave, the propagation of a beam can be represented by a list of *source* facets from which the beam originates, and a list of *sink* facets where the beam terminates. The notation ${}^{l}_{m}f^{j}$ is used to represent the jth sink facet in the particle mesh illuminated by a source facet f^k in the lth beam of the mth recursion. A visual representation of this is shown in Fig. 4(b). For clarity, the prescript notation will be temporarily omitted but reintroduced later for completeness.

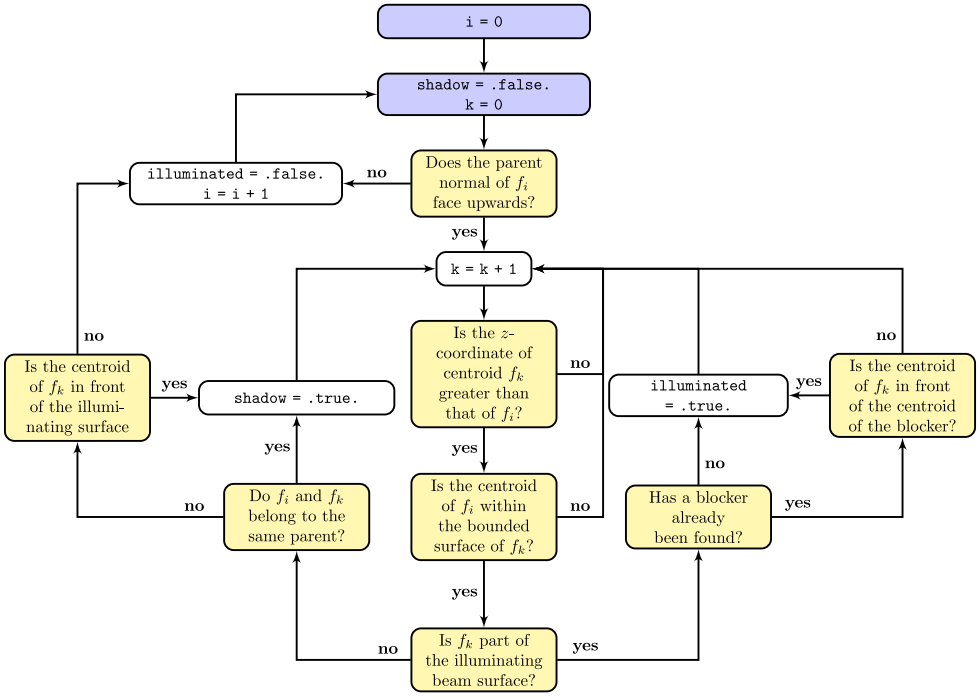

Fig. 6. Diagram summarising the ray backtracing algorithm. The algorithm determines if the centroid of f^i is within the bounded cross section of a source beam facet f^k when projected along the beam propagation direction.

The general goal here is to determine a mapping which connects the amplitude matrix at each of the source facets to each of the sink facets. To obtain the mapping, a novel ray backtracing algorithm is used in this work for maintaining stability when working with geometries with large numbers of facets. For each beam emitted from a parent structure, the coordinate system is rotated such that the propagation direction lies along the $-\hat{\mathbf{z}}$ axis. Since there is only one propagation direction, rays may be "backtraced" as an auxiliary measure from the centroid of each facet f^i along the reversed direction, which in this case is the $+\hat{\mathbf{z}}$ axis. If the backtraced ray intersects within the bounded cross section of a facet that was not part the source (ie. not in the set of values f^k), then f^i is determined to be not illuminated. If the backtraced ray intersects within the bounded cross section of a source facet, then f^i is appended to the list of sink facets. The process is shown in Fig. 5, whereby rays are backtraced upwards to determine if they intersect with the illuminating parent. A flow diagram summary of the algorithm is shown in Fig. 6. It should be noted that the particle mesh should be sufficiently discretised in order to conserve energy.

For particles with surface roughness, oblique incidence can be difficult to model with GO. In this scenario, the effect of small bumps in the surface geometry is magnified, which can cause small peaks in the surface geometry to produce large occluded shadow regions. This is problematic because GO assumes a coherent plane wave, which is no longer satisfied. Furthermore, GO predicts total internal reflection for very oblique incidence and therefore careful modelling of these cases is important for maintaining conservation of energy. To circumvent this, some rays are allowed to artificially pass through facets which belong to the same parent. In this way, beams at oblique incidence are allowed to glide over the bumps of a rough surface. An example of this is shown in the upper left of Fig. 5.

For incidence $\hat{\mathbf{K}}_\mathbf{0}$ in a medium with refractive index n_1, the refracted beam propagation direction $\hat{\mathbf{K}}'$ in a medium with refractive index n_2 is given by

$$\hat{\mathbf{K}}' = \frac{\sin(\theta_i - \theta_t)}{\sin\theta_i}\hat{\mathbf{N}} - \frac{\sin\theta_t}{\sin\theta_i}\hat{\mathbf{K}}_\mathbf{0}, \tag{4}$$

and the reflected beam propagation direction $\hat{\mathbf{K}}''$ is given by

$$\hat{\mathbf{K}}'' = \hat{\mathbf{K}}_\mathbf{0} + 2\cos\theta_i\hat{\mathbf{N}}, \tag{5}$$

where $\hat{\mathbf{N}}$ is assumed to point towards $\hat{\mathbf{K}}_\mathbf{0}$ (Appendix). If the angle of incidence is greater than the critical angle, no refracted beam is produced. At each recursion, a beam is propagated in the $-\hat{\mathbf{z}}$ direction from the source along the path of each backtraced ray. For each reflection and refraction process, the amplitude matrix at f^j is computed in a 3-step process:

1. First, for each sink facet f^j, the distance along the $\hat{\mathbf{z}}$-axis from its centroid to the centroid of the corresponding source facet f^k is used as the path length δ^j of the backtraced ray. Only this distance and the amplitude matrix at the source facet is needed to compute the amplitude matrix at the sink facet, which is a corollary of Snell's law and is illustrated in Fig. 4(b). The amplitude matrices are simply related by a phase factor $\exp(ik_0 n\delta^j)$.
2. Second, for each beam, the angle of incidence θ_i^j and refractive indices are used to compute the Fresnel matrix. At f^j, the Fresnel reflection matrix $\mathbf{F}_\mathbf{R}^\mathbf{j}$ and Fresnel transmission matrix $\mathbf{F}_\mathbf{T}^\mathbf{j}$ are given by
$$\mathbf{F}_\mathbf{R}^\mathbf{j} = \begin{pmatrix} r_\parallel^j & 0 \\ 0 & r_\perp^j \end{pmatrix}, \quad \mathbf{F}_\mathbf{T}^\mathbf{j} = \begin{pmatrix} t_\parallel^j & 0 \\ 0 & t_\perp^j \end{pmatrix}, \tag{6}$$
where $r_\parallel^j$, $r_\perp^j$, $t_\parallel^j$, and $t_\perp^j$ are the Fresnel amplitude coefficients of reflection and transmission. In contrast to the propagation direction of each beam, the Fresnel amplitude coefficients are calculated using the angle of incidence between the incident propagation vector and the local surface normal $\hat{\mathbf{n}}^\mathbf{j}$. The angle of incidence θ_i^j, angle of transmission θ_t^j, and refractive indices n_1 and n_2 are related via Snell's law. The amplitude matrices of the reflected and transmitted beams are computed by multiplying the incident amplitude matrices with the corresponding Fresnel matrices.
3. Third, the amplitude matrices of each beam are rotated into the new plane of incidence. The new plane contains the incident propagation vector $\hat{\mathbf{K}}_\mathbf{0}$ and the normal to the surface at the point of intersection $\hat{\mathbf{n}}$. The amplitude matrix is rotated about the incident propagation vector by the angle made between the old

and new incidence planes. For an incident propagation vector $\hat{\mathbf{K}}_\mathbf{0}$, and unit vectors perpendicular to the old and new planes given by $\hat{\mathbf{e}}^\mathbf{i}_\perp$ and $\hat{\mathbf{e}}^\mathbf{s}_\perp$, respectively, the new amplitude matrix is found by applying a rotation matrix $\mathbf{R^j}$, which is given by [47],

$$\mathbf{R^j} = \begin{pmatrix} \hat{\mathbf{e}}^\mathbf{i}_\perp \cdot \hat{\mathbf{e}}^\mathbf{s}_\perp & -\hat{\mathbf{e}}^\mathbf{s}_\perp \cdot (\hat{\mathbf{K}}_\mathbf{0} \times \hat{\mathbf{e}}^\mathbf{i}_\perp) \\ \hat{\mathbf{e}}^\mathbf{s}_\perp \cdot (\hat{\mathbf{K}}_\mathbf{0} \times \hat{\mathbf{e}}^\mathbf{i}_\perp) & \hat{\mathbf{e}}^\mathbf{i}_\perp \cdot \hat{\mathbf{e}}^\mathbf{s}_\perp \end{pmatrix}. \tag{7}$$

Therefore, the reflected and transmitted amplitude matrices at f^j are given by

$$\mathbf{S^j_R} = \mathbf{R^j} \cdot \mathbf{F^j_R} \cdot \exp(ik_0 n\delta^j) \cdot \mathbf{S^k}, \tag{8}$$

and

$$\mathbf{S^j_T} = \mathbf{R^j} \cdot \mathbf{F^j_T} \cdot \exp(ik_0 n\delta^j) \cdot \mathbf{S^k}, \tag{9}$$

respectively, where $\mathbf{S^k}$ is the amplitude matrix at the source facet. In the next step, the surface near-field is mapped to the far-field using a diffraction integral equation.

2.3. Far-field mapping

During the far-field mapping process, the near-field on the particle surface is integrated to calculate the electric field at a position in the far-field. The diffracted field is assumed to obey the Sommerfeld radiation condition [41]. There exist both volume and surface integral equations for computing the diffracted far-fields. The surface integral method is used here for its superior computationally efficiency and will be discussed in greater detail below. This section is based on theories described by Macke [31] and Karczewski [39] for electromagnetic diffraction at an aperture for an incident monochromatic plane wave. In this case, the incident electromagnetic field is described by

$$\begin{aligned} \mathbf{E}^{(i)}(\mathbf{r}) &= \mathbf{A}e^{ik_0(\hat{\mathbf{K}}\cdot\mathbf{r})}, \\ \mathbf{H}^{(i)}(\mathbf{r}) &= \mathbf{B}e^{ik_0(\hat{\mathbf{K}}\cdot\mathbf{r})}, \end{aligned} \tag{10}$$

where $\mathbf{E}^{(i)}$ and $\mathbf{H}^{(i)}$ are the incident electric and magnetic fields at position $\mathbf{r}$, $\mathbf{A}$ and $\mathbf{B}$ are complex vector amplitudes, and $\hat{\mathbf{K}} = (K_x, K_y, K_z)$ is the propagation vector. For a plane wave, $\mathbf{A}$ and $\mathbf{B}$ are related by $\mathbf{B} = \hat{\mathbf{K}}\times\mathbf{A}$. Imposing the Kirchhoff boundary conditions on the aperture, which approximates the diffracted field on the aperture as that of the incident field, gives that

$$\begin{aligned} \mathbf{n}\times\mathbf{E} &= \mathbf{n}\times\mathbf{E}^{(i)}, \\ \mathbf{n}\times\mathbf{H} &= \mathbf{n}\times\mathbf{H}^{(i)}. \end{aligned} \tag{11}$$

In this case, the diffracted electric field due to an illuminated aperture S at a point $\mathcal{P}$ can be given by

$$\mathbf{E}(\mathcal{P}) = \nabla\times\mathbf{\Pi^{(i)}_m} - 1/k_0\nabla\times\nabla\times\mathbf{\Pi^{(i)}_e}, \tag{12}$$

with

$$\begin{aligned} \mathbf{\Pi^{(i)}_m} &= \frac{1}{4\pi}\iint_S \mathbf{n}\times\mathbf{E}^{(i)}(\mathcal{Q})\frac{e^{ik_0 r}}{r}dS, \\ \mathbf{\Pi^{(i)}_e} &= \frac{1}{4\pi}\iint_S \mathbf{n}\times\mathbf{H}^{(i)}(\mathcal{Q})\frac{e^{ik_0 r}}{r}dS, \end{aligned} \tag{13}$$

where r is the distance from a point on the aperture $\mathcal{Q}$ to the point $\mathcal{P}$, $\mathbf{\Pi^{(i)}_e}$ is the electric Hertz potential, and $\mathbf{\Pi^{(i)}_m}$ is the magnetic Hertz potential. For the case of an incident plane wave, Eq. (12) can be simplified in the far-field limit ($r \gg d, \lambda$) to [39]

$$\mathbf{E}(\mathcal{P}) = \hat{\mathbf{k}}\times(\mathbf{F}\times\mathbf{A}) + (\mathbf{F}\times\mathbf{B}) - \hat{\mathbf{k}}\cdot(\mathbf{F}\times\mathbf{B})\hat{\mathbf{k}}, \tag{14}$$

where

$$\mathbf{F} = C\mathbf{n}\iint_S e^{ik_0(\hat{\mathbf{K}}-\hat{\mathbf{k}})\cdot\mathbf{R}}dS, \quad C = \frac{ik_0 e^{ik_0 r_0}}{4\pi r_0}. \tag{15}$$

Here, $\hat{\mathbf{k}} = (k_x, k_y, k_z)$ is the unit vector from the point of integration over the aperture to the point of observation. It varies for each point of observation and as a function of position over the aperture. $\mathbf{R} = (R_x, R_y, R_z)$ is the position vector of each area element and r_0 is the distance from the centre of the aperture to the point of observation. A subtle point of interest here is that the distance r from $\mathcal{Q}$ to $\mathcal{P}$ has been removed and substituted for the distance r_0. By separating the components of the bracketed term in the integrand exponent, the physical representation of each term can be identified. Firstly, $\exp(ik_0\hat{\mathbf{K}}\cdot\mathbf{R})$ describes how the phase of the incoming plane wave varies across the aperture. Secondly, if the exponential term in C is included, $\exp(ik_0 r_0\hat{\mathbf{k}}\cdot\mathbf{R})$ describes (to a first-order approximation) the phase change of the diffracted wavelet from point $\mathcal{Q}$ to point $\mathcal{P}$. If the aperture is planar, the coordinate system may be rotated about the centre of the aperture so that the aperture lies in the xy plane. In this case, $R_z = 0$. Furthermore, if the incident wave can be assumed as a plane wave, it will be shown that the integral in Eq. (15) can be converted to a summation around the contour of the aperture [31,48]. This provides a computationally cheap method for mapping from the near to the far-fields. Under these constraints, Eq. (15) simplifies to

$$\mathbf{F} = C\mathbf{n}\iint_S e^{ik_0[(K_x-k_x)x'+(K_y-k_y)y']}dS. \tag{16}$$

Defining new constants $k'_x = k_0(K_x - k_x)$ and $k'_y = k_0(K_y - k_y)$, Eq. (16) becomes

$$\mathbf{F} = C\mathbf{n}\iint_S e^{i(k'_x x'+k'_y y')}dS. \tag{17}$$

Now, two new variables, P and Q, are introduced to apply Green's theorem to convert Eq. (17) to a line integral around the contour of the aperture. Choosing

$$Q = \frac{e^{i(k'_x x'+k'_y y')}}{2ik'_y}, \quad P = \frac{e^{i(k'_x x'+k'_y y')}}{2ik'_x}, \tag{18}$$

the integral $\mathbf{F}$ can be rewritten as

$$\mathbf{F} = C\mathbf{n}\iint_S\left(\frac{\partial Q}{\partial y'} + \frac{\partial P}{\partial x'}\right)dS = \oint_S\Big(Qdx' - Pdy'\Big), \tag{19}$$

where $dS = dx'dy'$, since the aperture is planar and located in the xy plane. For polygonal apertures with N vertices, Eq. (19) can be written as a summation over the contributions from each edge:

$$\mathbf{F} = C\mathbf{n}\sum_{j=1}^{N}\int_j^{j+1}\Big(Qdx' - Pdy'\Big), \tag{20}$$

where the integration limits indicate that the integral should be evaluated for the edge between vertices j and $j+1$. Next, expressions for x' and y' along the edge between the two vertices are derived. The gradient and reciprocal gradient between the two vertices are

$$m_j = \frac{y_{j+1}-y_j}{x_{j+1}-x_j}, \quad n_j = \frac{x_{j+1}-x_j}{y_{j+1}-y_j}, \tag{21}$$

respectively. Using these expressions, the y' dependence in Q can be rewritten in terms of x' and vice versa for P. Eq. (20) then becomes

$$\mathbf{F} = C\mathbf{n}\sum_{j=1}^{N}\int_j^{j+1}\left(\frac{e^{i\{k'_y[y_j+(x'-x_j)m_j]+k'_x x'\}}}{2ik'_y}dx' - \frac{e^{i\{k'_x[x_j+(y'-y_j)n_j]+k'_y y'\}}}{2ik'_x}dy'\right). \tag{22}$$

After integration and some rearranging, the final expression is given by

$$\mathbf{F} = C\mathbf{n}\sum_{j=1}^{N}\alpha[e^{i\delta} - e^{i(\delta+\omega_1)}] - \beta[e^{i\delta} - e^{i(\delta+\omega_2)}], \tag{23}$$

with, $\alpha = \frac{1}{2k'_y(k'_y m_j + k'_x)}$, $\beta = \frac{1}{2k'_x(k'_x n_j + k'_y)}$, $\delta = k'_x x_j + k'_y y_j$, $\omega_1 = (x_{j+1} - x_j)(k'_y m_j + k'_x)$, and $\omega_2 = (y_{j+1} - y_j)(k'_x n_j + k'_y)$. With this formulation, the integral in Eq. (15) representing the scalar Fraunhofer pattern can be readily evaluated to yield $\mathbf{F}$.

To determine $\mathbf{E}(\mathcal{P})$ from Eq. (14), further work must be done to account for the vector nature of the scattered light. For this, the

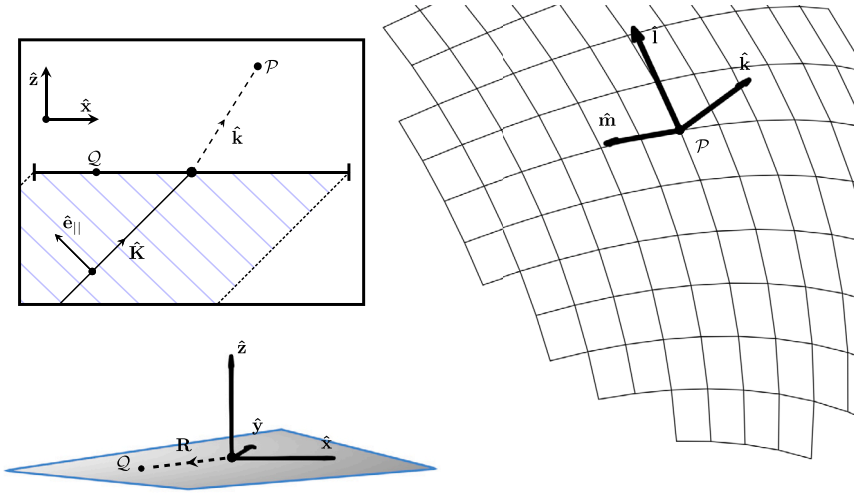

Fig. 7. The diffraction geometry. An incident beam is diffracted by a planar, polygonal aperture. The coordinate system has been rotated such that the aperture lies in the xy plane and the incident beam propagation vector $\hat{\mathbf{K}}$ and parallel field component $\hat{\mathbf{e}}_{\parallel}$ are aligned with the xz plane. The point of observation in the far-field is denoted by $\mathcal{P}$, and is located in the direction $\hat{\mathbf{k}}$ from the centre of the aperture. A grid structure is shown as an example of the different angular positions at which the far-field may be evaluated.

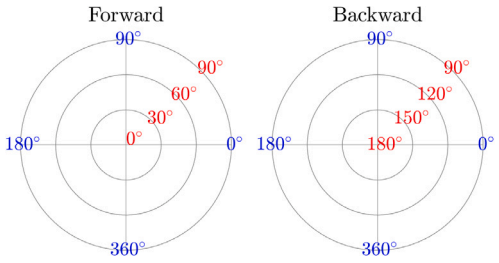

Fig. 8. Diagram depicting the azimuthal (blue) and scattering (red) scattering for 2-D polar plots in the forwards (left) and backwards (right) directions.

coordinate system is rotated about the $\hat{\mathbf{z}}$-axis such that $\hat{\mathbf{e}}_{\parallel}$ lies in the xz plane. By using the unitary property and relation between the incident propagation vector and the electric field component vectors:

$$\hat{\mathbf{K}}^2 = \hat{\mathbf{e}}_{\parallel}^2 = \hat{\mathbf{e}}_{\perp}^2 = 1, \quad \hat{\mathbf{K}} \times \hat{\mathbf{e}}_{\parallel} = \hat{\mathbf{e}}_{\perp}, \tag{24}$$

the x, y, and z components of the electric field components can be expressed in terms of $\hat{\mathbf{K}}$ by

$$\hat{\mathbf{e}}_{\parallel} = \frac{1}{\eta}\begin{pmatrix} K_z \\ 0 \\ -K_x \end{pmatrix}, \quad \hat{\mathbf{e}}_{\perp} = \frac{1}{\eta}\begin{pmatrix} -K_x K_y \\ \eta^2 \\ -K_y K_z \end{pmatrix}, \quad \eta = \sqrt{1 - K_y^2}. \tag{25}$$

For each point of observation in the far-field, two more unit vectors $\hat{\mathbf{l}}$ and $\hat{\mathbf{m}}$ are introduced to define the reference plane for which the electric field components will be calculated. If $\hat{\mathbf{k}}$, $\hat{\mathbf{l}}$, and $\hat{\mathbf{m}}$ are chosen as a triad of mutually orthogonal unit vectors, and $\hat{\mathbf{l}}$ is again chosen to lie in the xz plane, the components of $\hat{\mathbf{l}}$ and $\hat{\mathbf{m}}$ can be expressed in a similar manner in terms of $\hat{\mathbf{k}}$ by,

$$\hat{\mathbf{l}} = \frac{1}{\zeta}\begin{pmatrix} k_z \\ 0 \\ -k_x \end{pmatrix}, \quad \hat{\mathbf{m}} = \frac{1}{\zeta}\begin{pmatrix} -k_x k_y \\ \zeta^2 \\ -k_y k_z \end{pmatrix}, \quad \zeta = \sqrt{1 - k_y^2}. \tag{26}$$

A diagram illustrating the arrangement is shown in Fig. 7. In this way, it may be shown that [39], the far-field amplitude matrix defined with respect to the directions $\hat{\mathbf{l}}$ and $\hat{\mathbf{m}}$ is given by,

$$\mathbf{S_{far}} = 2F\begin{pmatrix} a & b \\ -b & a \end{pmatrix}\mathbf{S_{inc}}, \tag{27}$$

$$a = \frac{1}{2}\left(-k_z\sqrt{\eta/\zeta} - K_z\sqrt{\zeta/\eta}\,\right), \quad b = \frac{1}{2}\left(-k_x k_y\sqrt{\eta/\zeta} + K_x K_y\sqrt{\zeta/\eta}\,\right). \tag{28}$$

In the application considered here, the incident electric field is replaced by the amplitude matrix of a transmitted beam. Finally, 2 more rotation matrices are applied to obtain the electric field components with respect to static scattering planes in the original coordinate system.

1. First, for an incidence direction along the $-\hat{\mathbf{z}}$-axis, and scattering direction $\hat{\mathbf{k}}$ pointing from the particle centre of mass to the observation point, the scattering plane containing both these vectors has a normal given by $\hat{\mathbf{M}} = -\hat{\mathbf{z}} \times \hat{\mathbf{k}}$. To rotate the far-field components defined by Eq. (27) into this plane, the rotation matrix $\mathbf{R_1}$ is applied to rotate the electric field components about the direction $\hat{\mathbf{k}}$ from the plane perpendicular to $\hat{\mathbf{m}}$ to the plane perpendicular to $\hat{\mathbf{M}}$, with
$$\mathbf{R_1} = \begin{pmatrix} \hat{\mathbf{m}} \cdot \hat{\mathbf{M}} & -\hat{\mathbf{M}} \cdot (\hat{\mathbf{k}} \times \hat{\mathbf{m}}) \\ \hat{\mathbf{M}} \cdot (\hat{\mathbf{k}} \times \hat{\mathbf{m}}) & \hat{\mathbf{m}} \cdot \hat{\mathbf{M}} \end{pmatrix}. \tag{29}$$
2. Second, the initial incident amplitude matrix is pre-rotated about the $\mathbf{z}$-axis from the yz plane into the scattering plane, which allows for a direct comparison between the incident and scattered field. For each azimuthal scattering direction, each transmitted beam is premultiplied by the rotation matrix $\mathbf{R_0}$:
$$\mathbf{R_0} = \begin{pmatrix} -\sin\phi & -\cos\phi \\ \cos\phi & -\sin\phi \end{pmatrix}, \tag{30}$$
where ϕ is measured as shown in Fig. 1. Close to the direct forwards and backwards directions, ϕ and thus $\mathbf{R_0}$ are not well defined. Therefore, in these cases the PBT obtains $\mathbf{R_0}$ from the values of ϕ at $\theta = 1°$. The final expression for the diffracted far field components is given by
$$\mathbf{S_{far}} = \mathbf{R_1} \cdot 2F\begin{pmatrix} a & b \\ -b & a \end{pmatrix}\mathbf{S_T} \cdot \mathbf{R_0}. \tag{31}$$

To summarise, Eq. (27) relates the parallel and perpendicular diffracted far-field components from a planar aperture for an incident plane wave, with the scalar Fraunhofer pattern F obtainable from Eq. (23). By a summation over all diffracted beams, a complete description for the electric field in the far-field is obtained as an amplitude matrix as a function of observation position, which can be written mathematically as

$$\mathbf{S_{far}} = \sum_{m=0}^{M}\sum_{l=1}^{L(m)}\sum_{j(l)} {}^{\mathbf{l}}_{\mathbf{m}}\mathbf{S}^{\mathbf{j}}_{\mathbf{far}}, \tag{32}$$

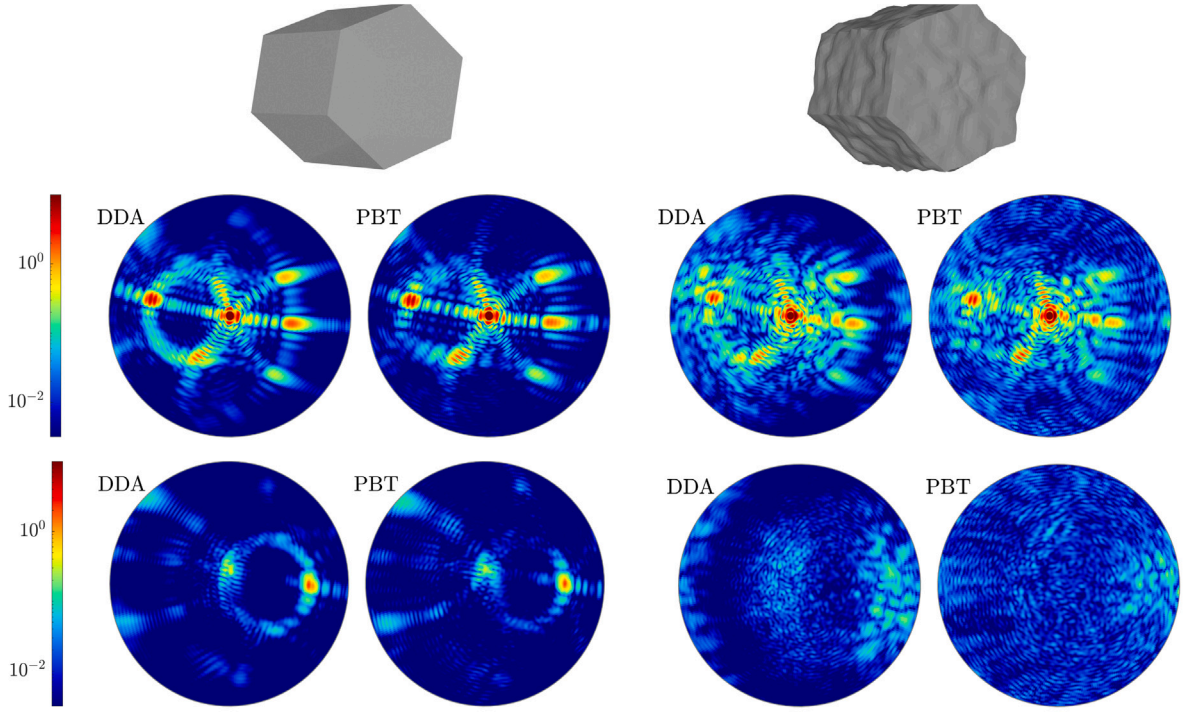

Fig. 9. The logarithms of the 2-D phase functions for smooth (left and middle-left) and rough (middle-right and right) compact columns with refractive index 1.31 + 0i. The upper and lower rows of polar plots correspond to the forwards and backwards scattering, respectively, as depicted in the schematic of Fig. 8. The particles and their orientations as viewed along the direction of incidence are shown for reference.

where M is the total number of recursions, $L(m)$ is the total number of beams at the mth recursion, $j(l)$ are the indices of facets illuminated by the lth beam of the mth recursion, and ${}^{l}_{m}\mathbf{S}^{j}_{far}$ are the far field amplitude matrices for each transmitted amplitude matrix ${}^{l}_{m}\mathbf{S}^{j}_{T}$. Babinet's principle is used to account for the scattering of light which is not directly incident upon the particle geometric cross section. The externally diffracted field is computed from the amplitude matrix at facets illuminated by the initial incident wave as described in Section 2.2.2 but without applying the Fresnel matrices. The total scattered field is obtained by a summation of the diffraction of surface fields due to transmission and reflection with external diffraction. Finally, the Mueller matrix can be determined from the total amplitude matrix by well-known relations (ie. Hovenier, Bohren & Huffman, Van de Hulst [47,49,50]).

3. Results

In this section, the results from the PBT for smooth and rough hexagonal columns with length $l = 10$ μm, and radius $r = 5$ μm are presented. Rough particles are generated using Gaussian random roughness with correlation length 0.5 μm and standard deviation 0.1 μm as described by Collier et al. [43]. The accuracy of the results is measured by comparison with the Amsterdam DDA (ADDA) code [19], which discretises the scatterer into an array of dipoles. The accuracy of ADDA has been reported several times in the literature and here the results are considered as a benchmark for comparison [19,51–53]. While the formulation of the DDA method is a direct implication of the Maxwell equations, an exact solution is derived according to the set of dipoles rather than the original scatterer. Therefore, in this study two main criteria are considered to accurately represent the particle by an array of dipoles. Firstly, the number of dipoles per wavelength d is chosen in accordance with the ADDA 'rule-of-thumb' which requires that $d \leq 10/(\lambda|n|)$. Secondly, d is required to be smaller than any characteristic sizes of the particle. For particles with Gaussian roughness, d is chosen such that at least 10 dipoles per correlation length are present.

The logarithms of the 2-D phase functions for non-absorbing smooth and rough hexagonal columns in a fixed orientation with refractive index $n = 1.31+0\mathrm{i}$ are shown in Fig. 9. The results for other elements of the Mueller matrix for the smooth and rough particles in the same orientation with refractive index $n = 1.31+0\mathrm{i}$ are shown in Fig. 11. The particle orientation is produced by first aligning the prism axis with the z-axis, then by rotating with Euler angles $\alpha = 0°$, $\beta = 30°$, $\gamma = 20°$ according to the "zyz-notation" as given in [54]. The azimuthal and polar scattering angles may be inferred from the diagram shown in Fig. 8. The PBT method produces results in $\sim 1/1000$th of the computation time required for the DDA computations. The 1-D phase function is computed by integration over phi using a 3-point Lagrange polynomial interpolation method [55]. The results for 3 sets of refractive indices in the same orientation are shown in Fig. 10. For the rough particles geometries, a comparison with GO is included. The residual σ is computed using $\sigma = (S_{ij}^{(pbt)} - S_{ij}^{(dda)})$, and the normalised residual $\overline{\sigma} = \sigma / S_{ij}^{(dda)}$, where S_{ij} corresponds to an element of the Mueller matrix. Table 1 summarises the values for various integrated scattering parameters of interest. By computing the mean values averaged over the smooth and rough particle configurations, the errors in the asymmetry parameter, and scattering and extinction efficiencies are −1.0%, −1.4%, −1.2%, respectively. For the smooth non-absorbing ($n = 1.31+0\mathrm{i}$) particle, the PBT patterns in Fig. 9 closely resemble those computed with DDA. In the direct forwards scattering, a strong peak is observed, corresponding to external diffraction combined with any beam entering and being transmitted through a pair of parallel surfaces. At approximately 60° scattering angles, several regions of high scattering intensity are observed, which correspond to transmitted beams undergoing 1 or 2 internal reflections. The PBT method shows a particular improvement over GO in this region, which increases the accuracy of the asymmetry parameter. In the backscattering hemisphere, external reflection combined with a transmitted beam undergoing total internal reflection is observed at approximately 120°. In general, PBT computations are able to reproduce many of the key features seen in the DDA results. However, the accuracy decreases towards the backscattering, which indicates room for improvement in the near-field computation for non-absorbing particles as seen here.

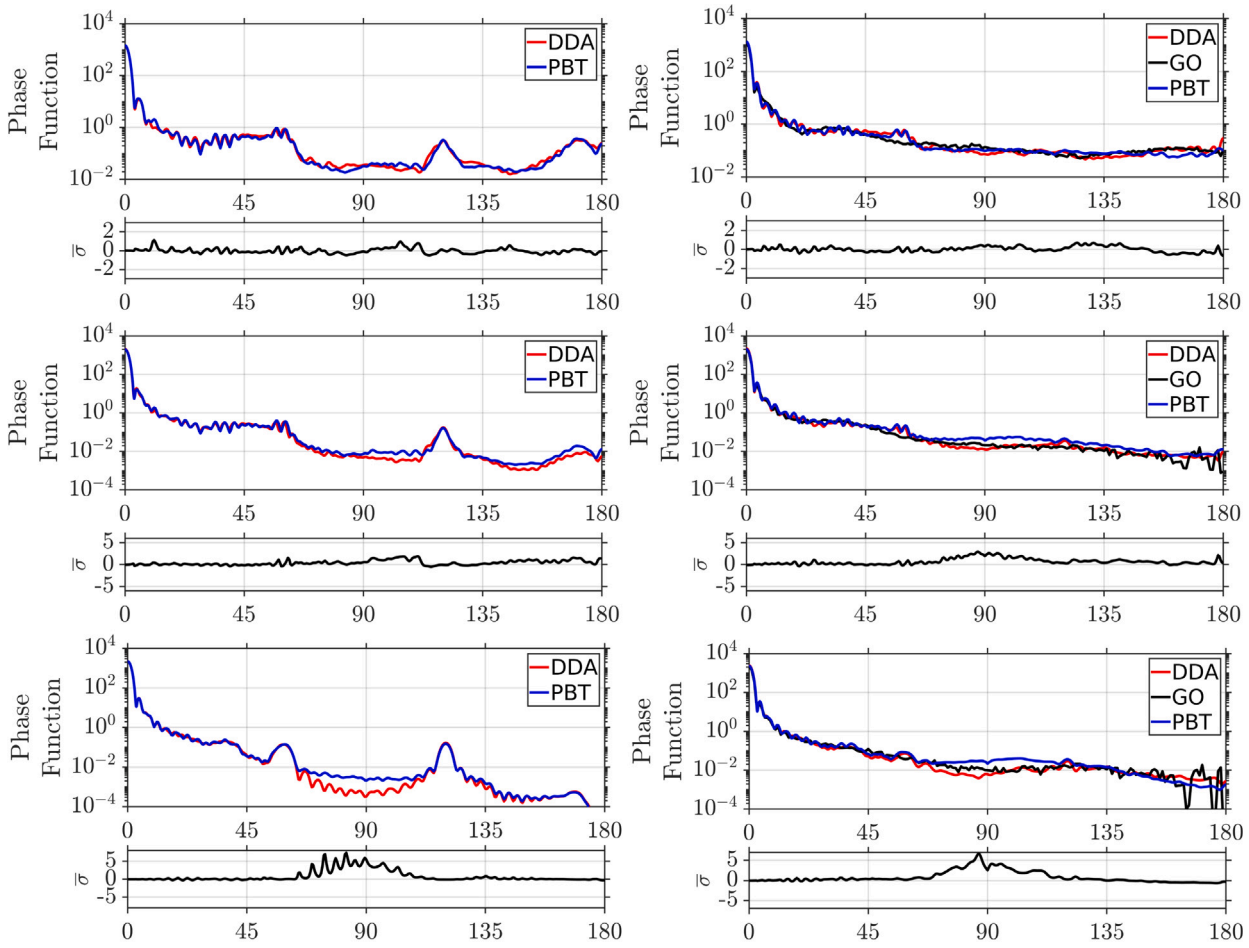

Fig. 10. The 1-D phase function for smooth (left) and rough (right) compact columns. Rows correspond to refractive indices 1.31 + 0i, 1.31 + 0.01i, and 1.31 + 0.1i, respectively. The particle orientation is the same as shown in Fig. 9.

Table 1
Summary of the asymmetry parameter g, scattering efficiency Q_{sca}, and extinction efficiency Q_{ext} computed with the DDA and PBT methods for the smooth and rough particles in the orientation as shown in Fig. 9.

	n	$g^{(dda)}$	$g^{(pbt)}$	$\frac{g^{(pbt)}-g^{(dda)}}{g^{(dda)}}$ [%]	$Q_{sca}^{(dda)}$	$Q_{sca}^{(pbt)}$	$\frac{Q_{sca}^{(pbt)}-Q_{sca}^{(dda)}}{Q_{sca}^{(dda)}}$ [%]	$Q_{ext}^{(dda)}$	$Q_{ext}^{(pbt)}$	$\frac{Q_{ext}^{(pbt)}-Q_{ext}^{(dda)}}{Q_{ext}^{(dda)}}$ [%]
Smooth	1.31 + 0i	0.807	0.820	+1.6	2.580	2.537	−1.7	2.580	2.537	−1.7
	1.31 + 0.01i	0.941	0.937	−0.4	1.363	1.407	+3.2	2.251	2.154	−4.3
	1.31 + 0.1i	0.967	0.966	−0.1	1.112	1.057	−4.9	2.111	2.090	−1.0
Rough	1.31 + 0i	0.769	0.762	−0.9	2.183	2.142	−1.9	2.183	2.142	−1.9
	1.31 + 0.01i	0.941	0.906	−3.7	1.278	1.285	+0.5	2.236	2.251	+0.7
	1.31 + 0.1i	0.969	0.945	−2.5	1.177	1.135	−3.6	2.244	2.266	+1.0

The scattered intensities for absorbing particles are shown in the 2nd and 3rd rows of Fig. 10. The PBT results show exceptional agreement in the forward scattering, with a mean normalised residual of 2% for $\theta < 60°$. The PBT overestimates the scattered intensity around 90°, which could be a limitation of the surface integral diffraction method employed. However, the effect of this on the asymmetry parameter should be small. For the weakly absorbing particles ($n = 1.31+0.01i$), the PBT shows an overestimation in the back-scattered intensity, which is likely due to an oversimplification of the propagation of light as a coherent plane wave in lossy media. In fact, the light propagates as an incoherent plane wave in this case [29,56], which is not fully accounted for in this model. For the strongly absorbing particles ($n = 1.31+0.1i$), the scattering is dominated by external diffraction combined with external reflection. The PBT overestimates the side-scattering for rough absorbing particles. It is thought that a more accurate results could be achieved by improving the near-field approximation, particularly at areas of the surface occluded by the roughness.

4. Summary and conclusions

In this work, a new physical-optics hybrid method is described. The method is designed specifically for the computation of single-scattering properties of particles with complex shapes, including surface roughness. By combining geometric optics with a novel ray backtracing technique, the near-field on the surface of the particle is computed. A surface integral equation is then used to compute the scattered far-field, yielding the full Mueller matrix and optical parameters of interest. Fixed orientation computations for smooth and roughened hexagonal columns with 3 different levels of absorption are shown to compute the asymmetry parameter, and scattering and extinction efficiencies with mean errors of −1.0%, −1.4%, −1.2%, respectively, in a computation time reduced by 3 orders of magnitude. The accuracy of the method is expected to improve when extended to random orientation. In addition, the physical-optics nature of the technique allows the user to compute

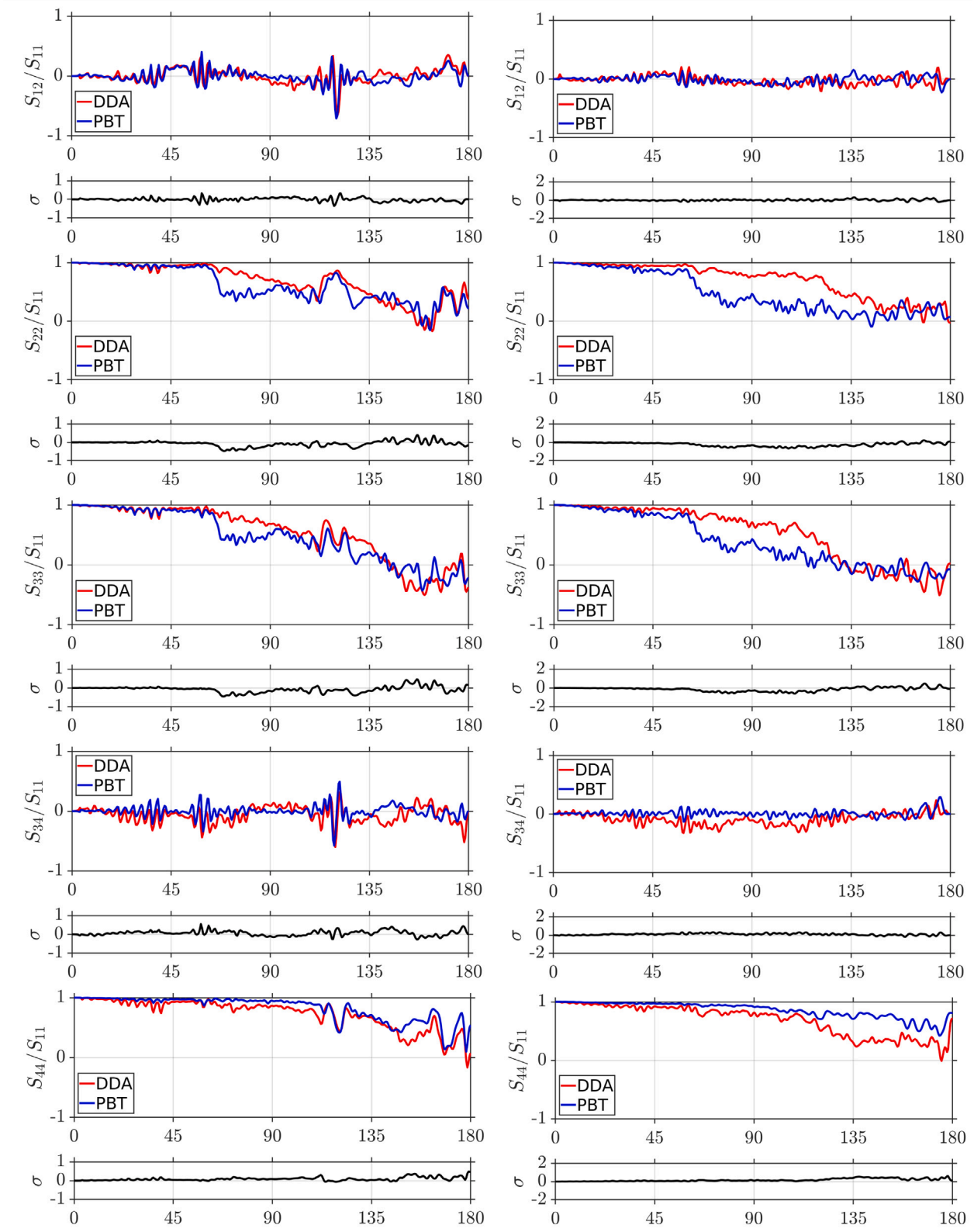

Fig. 11. Other elements of the Mueller matrix for smooth (left) and rough (right) compact columns with refractive index 1.31 + 0i in the same orientation as shown in Fig. 9.

the 2-dimensional scattered field at arbitrary scattering angles for particles in fixed orientations. Such an approach may provide a useful tool for calibrating instruments with specific angular detection range and resolution, and for interpretation of detected scattering patterns. The method presented in this work can be used to compute single particle scattering matrices and integrated parameter databases for particles well defined with respect to size, shape, surface properties, and refractive index. The application of such databases includes radiative transfer computations for climate models, and for calibration of instruments which use light scattering measurements for particle detection and

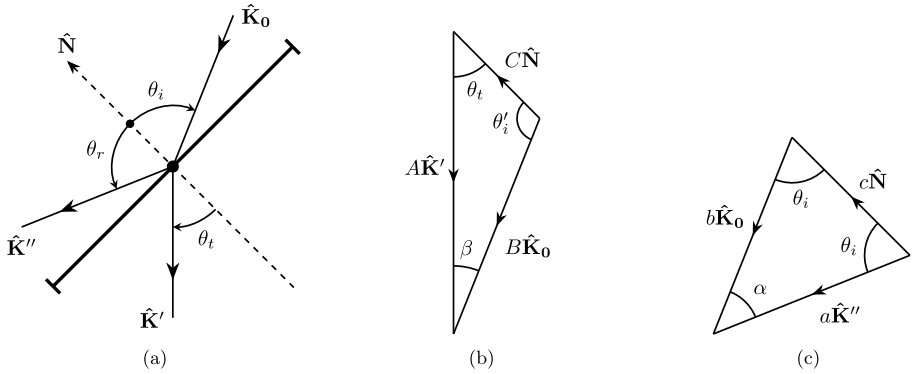

Fig. 12. (a) The geometry of the reflection and refraction at an interface. (b) The vector triangle formed between the incident propagation direction, the refracted propagation direction, and the surface normal. (c) The vector triangle formed between the incident propagation direction, the reflected propagation direction, and the surface normal.

sizing. The method shows improved accuracy over GO, which makes it a favourable approach for larger particles, where numerically exact methods cannot be applied. This work takes one step closer towards modelling particles with physical (rather than stochastic) roughness within the framework of a physical-optics hybrid method. The method stands as a versatile tool for the fast and quantitative study of light scattering from particles with size parameter much larger than the wavelength.

CRediT authorship contribution statement

H. Ballington: Writing – review & editing, Writing – original draft, Visualization, Validation, Software, Methodology, Investigation, Formal analysis, Data curation, Conceptualization. **E. Hesse:** Writing – review & editing, Validation, Supervision, Project administration, Funding acquisition.

Declaration of competing interest

The authors declare that they have no known competing financial interests or personal relationships that could have appeared to influence the work reported in this paper.

Data availability

Data will be made available on request.

Acknowledgements

The authors thank A. Penttilä for providing codes for mesh conversion. H. Ballington and E. Hesse acknowledge support by the Natural Environment Research Council (NERC), United Kingdom, grant NE/T00147X/1.

Appendix. Propagation direction

The expressions for the refracted and reflected propagation directions, $\hat{\mathbf{K}}'$ and $\hat{\mathbf{K}}''$, respectively, can be derived using vector triangles and the sine rule as shown in Fig. 12.

A.1. Refracted propagation direction

As shown in Fig. 12(b), a vector triangle can be formed such that

$$A\hat{\mathbf{K}}' = B\hat{\mathbf{K}}_\mathbf{0} - C\hat{\mathbf{N}}, \tag{33}$$

where A, B, and C are unknown lengths. Using the sine rule, the unknown lengths can be related to the angles of the triangle by

$$\frac{A}{\sin\theta_i'} = \frac{B}{\sin\theta_t} = \frac{C}{\sin\beta}, \tag{34}$$

where $\theta_i' = \pi - \theta_i$, and $\beta = \theta_i - \theta_t$. Substituting Eq. (34) into Eq. (33) gives

$$A\hat{\mathbf{K}}' = A\frac{\sin\theta_t}{\sin\theta_i'}\hat{\mathbf{K}}_\mathbf{0} - A\frac{\sin(\theta_i-\theta_t)}{\sin\theta_i'}\hat{\mathbf{N}}, \tag{35}$$

which may be rewritten as

$$\hat{\mathbf{K}}' = \frac{\sin(\theta_i-\theta_t)}{\sin\theta_i}\hat{\mathbf{N}} - \frac{\sin\theta_t}{\sin\theta_i}\hat{\mathbf{K}}_\mathbf{0}. \tag{36}$$

For generality, the angles of incidence and transmission may be rewritten in terms of $\hat{\mathbf{K}}_\mathbf{0}$, $\hat{\mathbf{N}}$, and the refractive indices, n_1 and n_2. The double angle formula may then be used to expand the bracketed term, which gives

$$\hat{\mathbf{K}}' = \left(\cos\theta_t - \cos\theta_i\frac{\sin\theta_t}{\sin\theta_i}\right)\hat{\mathbf{N}} - \frac{\sin\theta_t}{\sin\theta_i}\hat{\mathbf{K}}_\mathbf{0}. \tag{37}$$

Snell's law gives that

$$\frac{\sin\theta_t}{\sin\theta_i} = \frac{n_1}{n_2}, \quad \cos\theta_t = \sqrt{1-\frac{n_1^2}{n_2^2}\left(1-\cos^2\theta_i\right)}, \tag{38}$$

which allows Eq. (37) to be written as

$$\hat{\mathbf{K}}' = \sqrt{1-\frac{n_1^2}{n_2^2}\left(1-\cos^2\theta_i\right)}\hat{\mathbf{N}} - \frac{n_1}{n_2}\left(\cos\theta_i\hat{\mathbf{N}} + \hat{\mathbf{K}}_\mathbf{0}\right). \tag{39}$$

Finally, since $\cos\theta_i = -\hat{\mathbf{K}}_\mathbf{0}\cdot\hat{\mathbf{N}}$, this can be rewritten as

$$\hat{\mathbf{K}}' = \sqrt{1-\frac{n_1^2}{n_2^2}\left[1-(\hat{\mathbf{K}}_\mathbf{0}\cdot\hat{\mathbf{N}})^2\right]}\hat{\mathbf{N}} - \frac{n_1}{n_2}\left[\hat{\mathbf{K}}_\mathbf{0} - (\hat{\mathbf{K}}_\mathbf{0}\cdot\hat{\mathbf{N}})\hat{\mathbf{N}}\right]. \tag{40}$$

A.2. Reflected propagation direction

As shown in Fig. 12(c), a vector triangle can be formed such that

$$a\hat{\mathbf{K}}'' = b\hat{\mathbf{K}}_\mathbf{0} + c\hat{\mathbf{N}}, \tag{41}$$

where a, b, and c are unknown lengths. Using the sine rule, the unknown lengths can be related to the angles of the triangle by

$$\frac{a}{\sin\theta_i} = \frac{b}{\sin\theta_i} = \frac{c}{\sin\alpha}, \tag{42}$$

where $\alpha = \pi - 2\theta_i$. Substituting Eq. (42) into Eq. (41) gives

$$a\hat{\mathbf{K}}'' = a\hat{\mathbf{K}}_\mathbf{0} + a\frac{\sin(\pi - 2\theta_i)}{\sin\theta_i}\hat{\mathbf{N}}, \tag{43}$$

which may be rewritten as

$$\hat{\mathbf{K}}'' = \hat{\mathbf{K}}_\mathbf{0} + \frac{\sin(\pi - 2\theta_i)}{\sin\theta_i}\hat{\mathbf{N}}. \tag{44}$$

Using the double angle formula to expand the bracketed term, this simplifies to

$$\hat{\mathbf{K}}'' = \hat{\mathbf{K}}_\mathbf{0} + 2\cos\theta_i\hat{\mathbf{N}}. \tag{45}$$

Finally, since $\cos\theta_i = -\hat{\mathbf{K}}_\mathbf{0} \cdot \hat{\mathbf{N}}$, this may also be rewritten as

$$\hat{\mathbf{K}}'' = \hat{\mathbf{K}}_\mathbf{0} - 2(\hat{\mathbf{K}}_\mathbf{0} \cdot \hat{\mathbf{N}})\hat{\mathbf{N}}. \tag{46}$$

References

[1] Márquez-Islas R, et al. Visual assessment of blood plasma versus optical transmittance and refractive index measurements for quantifying lipemia. Diagnostics 2022;12. http://dx.doi.org/10.3390/diagnostics12020510.

[2] Gienger J, et al. Assessment of deformation of human red blood cells in flow cytometry: Measurement and simulation of bimodal forward scatter distributions. Biomed Opt Express 2019;10:4531. http://dx.doi.org/10.1364/boe.10.004531.

[3] Barone T, et al. Calibration of the cloud and aerosol spectrometer for coal dust composition and morphology. Adv Powder Technol 2019;30(9):1805–14. http://dx.doi.org/10.1016/j.apt.2019.05.023.

[4] Stopford C, et al. Real-time detection of airborne asbestos by light scattering from magnetically re-aligned fibers. Opt Express 2013;21(9):11356–67. http://dx.doi.org/10.1364/OE.21.011356.

[5] Ruiter S, et al. Exposure monitoring strategies for applying low-cost PM sensors to assess flour dust in industrial bakeries. Ann Work Expo Health 2023;67(3):379–91. http://dx.doi.org/10.1093/annweh/wxac088.

[6] Powers JG, et al. The weather research and forecasting model: Overview, system efforts, and future directions. Bull Am Meteorol Soc 2017;98:1717–37. http://dx.doi.org/10.1175/BAMS-D-15-00308.1.

[7] Kaye PH, et al. Classifying atmospheric ice crystals by spatial light scattering. Opt Lett 2008;33(13):1545–7. http://dx.doi.org/10.1364/OL.33.001545.

[8] Giri R, et al. Generation of aerosol-particle light-scattering patterns from digital holograms. Opt Lett 2019;44:819. http://dx.doi.org/10.1364/ol.44.000819.

[9] Winker DM, Hunt WH, McGill MJ. Initial performance assessment of CALIOP. Geophys Res Lett 2007;34(19). http://dx.doi.org/10.1029/2007GL030135.

[10] Waterman PC. Matrix formulation of electromagnetic scattering. 1965.

[11] Mishchenko MI, Travis LD, Mackowski DW. T-matrix computations of light scattering by nonspherical particles: A review. J Quant Spectrosc Radiat Transfer 1996;55:535–75. http://dx.doi.org/10.1016/0022-4073(96)00002-7.

[12] Doicu A, Eremin Y, Wriedt T. Acoustic and electromagnetic scattering analysis using discrete sources. 2000.

[13] Yee K. Numerical solution of initial boundary value problems involving Maxwell's equations in isotropic media. IEEE Trans Antennas and Propagation 1966;14(3):302–7. http://dx.doi.org/10.1109/TAP.1966.1138693.

[14] Yang P. Finite-difference time domain method for light scattering by small ice crystals in three-dimensional space. J Opt Soc Amer A (13).

[15] Sun W, Fu Q, Chen Z. Finite-difference time-domain solution of light scattering by dielectric particles with a perfectly matched layer absorbing boundary condition. Appl Opt 1999;38(15):3141–51. http://dx.doi.org/10.1364/AO.38.003141.

[16] Purcell EM, Pennypacker CR. Scattering and adsorption of light by nonspherical dielectric grains. Astrophys J 1973;186:705–14. http://dx.doi.org/10.1086/152538.

[17] Draine BT. The discrete-dipole approximation and its applications to interstellar graphite grains. Astrophys J 1988;333:848–72. http://dx.doi.org/10.1086/166795.

[18] Goedecke GH, O'Brien SG. Scattering by irregular inhomogeneous particles via the digitized Green's function algorithm. Appl Opt 1988;27(12):2431–8. http://dx.doi.org/10.1364/AO.27.002431.

[19] Yurkin MA, Hoekstra AG. The discrete-dipole-approximation code ADDA: Capabilities and known limitations. J Quant Spectrosc Radiat Transfer 2011;112(13):2234–47. http://dx.doi.org/10.1016/j.jqsrt.2011.01.031, Polarimetric Detection, Characterization, and Remote Sensing.

[20] Wendling P, Wendling R, Weickmann HK. Scattering of solar radiation by hexagonal ice crystals. Appl Opt 1979;18(15):2663–71. http://dx.doi.org/10.1364/AO.18.002663.

[21] Cai Q, Liou K-N. Polarized light scattering by hexagonal ice crystals: Theory. Appl Opt 1982;21(19):3569–80. http://dx.doi.org/10.1364/AO.21.003569.

[22] Muinonen K, Lumme K, Peltoniemi J, Irvine WM. Light scattering by randomly oriented crystals. Appl Opt 1989;28(15):3051–60. http://dx.doi.org/10.1364/AO.28.003051.

[23] Takano Y, Liou K-N. Solar radiative transfer in cirrus clouds. Part I: Single-scattering and optical properties of hexagonal ice crystals. J Atmos Sci 1989;46(1):3–19. http://dx.doi.org/10.1175/1520-0469(1989)046<0003:SRTICC>2.0.CO;2.

[24] Macke A. Scattering of light by polyhedral ice crystals. Appl Opt 1993;32(15):2780–8. http://dx.doi.org/10.1364/AO.32.002780.

[25] Borovoi AG. Light scattering by large particles: Physical optics and the shadow-forming field. In: Kokhanovsky AA, editor. Light scattering reviews 8: Radiative transfer and light scattering. Berlin, Heidelberg: Springer Berlin Heidelberg; 2013, p. 115–38. http://dx.doi.org/10.1007/978-3-642-32106-1_3.

[26] Yang P, Liou KN. Light scattering by hexagonal ice crystals: Solutions by a ray-by-ray integration algorithm. J Opt Soc Amer A 1997;14(9):2278–89. http://dx.doi.org/10.1364/JOSAA.14.002278.

[27] Hesse E, Ulanowski Z. Scattering from long prisms computed using ray tracing combined with diffraction on facets. J Quant Spectrosc Radiat Transfer 2003;79–80:721–32. http://dx.doi.org/10.1016/S0022-4073(02)00317-5, Electromagnetic and Light Scattering by Non-Spherical Particles.

[28] Borovoi AG, Grishin IA. Scattering matrices for large ice crystal particles. J Opt Soc Amer A 2003;20(11):2071–80. http://dx.doi.org/10.1364/JOSAA.20.002071.

[29] Bi L, Yang P, Kattawar GW, Hu Y, Baum BA. Scattering and absorption of light by ice particles: Solution by a new physical-geometric optics hybrid method. J Quant Spectrosc Radiat Transfer 2011;112(9):1492–508. http://dx.doi.org/10.1016/j.jqsrt.2011.02.015.

[30] Konoshonkin AV, Kustova NV, Borovoi AG. Beam-splitting code for light scattering by ice crystal particles within geometric-optics approximation. J Quant Spectrosc Radiat Transfer 2015;164:175–83. http://dx.doi.org/10.1016/j.jqsrt.2015.06.008.

[31] Macke A, Mueller J, Raschke E. Single scattering properties of atmospheric ice crystals. J Atmos Sci 1996;53(19):2813–25. http://dx.doi.org/10.1175/1520-0469(1996)053<2813:SSPOAI>2.0.CO;2.

[32] Liu C, Panetta RL, Yang P. The effective equivalence of geometric irregularity and surface roughness in determining particle single-scattering properties. Opt Express 2014;22(19):23620–7. http://dx.doi.org/10.1364/OE.22.023620.

[33] Yang P, et al. Spectrally consistent scattering, absorption, and polarization properties of atmospheric ice crystals at wavelengths from 0.2 to 100 μm. J Atmos Sci 2013;70(1):330–47. http://dx.doi.org/10.1175/JAS-D-12-039.1.

[34] Saito M, Yang P. Oriented ice crystals: A single-scattering property database for applications to lidar and optical phenomenon simulations. J Atmos Sci 2019;76(9):2635–52. http://dx.doi.org/10.1175/JAS-D-19-0031.1.

[35] Saito M, et al. A comprehensive database of the optical properties of irregular aerosol particles for radiative transfer simulations. J Atmos Sci 2021;78(7):2089–111. http://dx.doi.org/10.1175/JAS-D-20-0338.1.

[36] Timofeev DN, et al. Light backscattering properties of distorted hexagonal atmospheric ice particles within the physical optics approximation. Atmos Ocean Opt 2022;35(2):158–63. http://dx.doi.org/10.1134/S1024856022020130.

[37] Hesse E, et al. Discussion of a physical optics method and its application to absorbing smooth and slightly rough hexagonal prisms. J Quant Spectrosc Radiat Transfer 2018;218:54–67. http://dx.doi.org/10.1016/j.jqsrt.2018.06.019.

[38] Ballington H. Parent Beam Tracer Code. 2024, https://github.com/hballington12/pbt.

[39] Karczewski B, Wolf E. Comparison of three theories of electromagnetic diffraction at an aperture.* Part I: Coherence matrices. J Opt Soc Am 1966;56(9):1207–14. http://dx.doi.org/10.1364/JOSA.56.001207.

[40] Yang P, Liou KN. Geometric-optics–integral-equation method for light scattering by nonspherical ice crystals. Appl Opt 1996;35:6568–84. http://dx.doi.org/10.1364/AO.35.006568.

[41] Sommerfeld A. Partial differential equations in physics. New York: Academic Press; 1949.

[42] Yurkin M, Hoekstra A. The discrete dipole approximation: An overview and recent developments. J Quant Spectrosc Radiat Transfer 2007;106(1):558–89. http://dx.doi.org/10.1016/j.jqsrt.2007.01.034, IX Conference on Electromagnetic and Light Scattering by Non-Spherical Particles.

[43] Collier C, et al. Effects of surface roughness with two scales on light scattering by hexagonal ice crystals large compared to the wavelength: DDA results. J Quant Spectrosc Radiat Transfer 2016;182:225–39. http://dx.doi.org/10.1016/j.jqsrt.2016.06.007.

[44] Taylor L. A beam tracing model for electromagnetic scattering by atmospheric ice crystals (Ph.D. thesis), University of Hertfordshire; 2016.

[45] Borovoi A, Konoshonkin A, Kustova N. The physical-optics approximation and its application to light backscattering by hexagonal ice crystals. J Quant Spectrosc Radiat Transfer 2014;146:181–9. http://dx.doi.org/10.1016/j.jqsrt.2014.04.030, Electromagnetic and Light Scattering by Nonspherical Particles XIV.

[46] Sheffer A. Model simplification for meshing using face clustering. Comput Aided Des 2001;33(13):925–34. http://dx.doi.org/10.1016/S0010-4485(00)00116-0.

[47] Hovenier JW, Mee C, Domke H. Transfer of polarised light in planetary atmospheres. Springer Dordrecht; 2004.
[48] Hesse E, et al. Modelling diffraction by facetted particles. J Quant Spectrosc Radiat Transfer 2012;113(5):342–7. http://dx.doi.org/10.1016/j.jqsrt.2011.11.017.
[49] Bohren CF, Huffman DR. Absorption and scattering of light by small particles. John Wiley & Sons; 1983.
[50] van de Hulst HC. Light scattering by small particles. Dover Publications; 1981.
[51] Yurkin M, Maltsev V, Hoekstra A. The discrete dipole approximation for simulation of light scattering by particles much larger than the wavelength. J Quant Spectrosc Radiat Transfer 2007;106(1):546–57. http://dx.doi.org/10.1016/j.jqsrt.2007.01.033, IX Conference on Electromagnetic and Light Scattering by Non-Spherical Particles.
[52] Penttilä A, et al. Comparison between discrete dipole implementations and exact techniques. J Quant Spectrosc Radiat Transfer 2007;106(1):417–36. http://dx.doi.org/10.1016/j.jqsrt.2007.01.026, IX Conference on Electromagnetic and Light Scattering by Non-Spherical Particles.
[53] Schmidt K, Yurkin MA, Kahnert M. A case study on the reciprocity in light scattering computations. Opt Express 2012;20(21):23253–74. http://dx.doi.org/10.1364/OE.20.023253.
[54] Mishchenko MI. Calculation of the amplitude matrix for a nonspherical particle in a fixed orientation. Appl Opt 2000;39(6):1026–31. http://dx.doi.org/10.1364/AO.39.001026.
[55] Hennion PE. Algorithm 77: Interpolation, differentiation, and integration. Commun ACM 1962;5(2):96. http://dx.doi.org/10.1145/366792.366811.
[56] Chang PC, Walker J, Hopcraft K. Ray tracing in absorbing media. J Quant Spectrosc Radiat Transfer 2005;96(3):327–41. http://dx.doi.org/10.1016/j.jqsrt.2005.01.001.